Infrared Physics & Technology 150 (2025) 105939

Contents lists available at ScienceDirect

Infrared Physics and Technology

journal homepage: www.elsevier.com/locate/infrared

Economical and easily implemented Vernier effect bubble microcavity FPI for strain sensing with extreme low-temperature cross-sensitivity

Chao Liu [a,*], Jianxin Wang [a], Jingwei Lv [a], Xinping Song [a], Wei Liu [a], Qiang Liu [a], Renfeng Li [a], Liangliang Li [a], Zao Yi [b], Paul K. Chu [c]

[a] School of Physics and Electronic Engineering, Northeast Petroleum University, Daqing 163318, China
[b] Joint Laboratory for Extreme Conditions Matter Properties, Southwest University of Science and Technology, Mianyang 621010, China
[c] Department of Physics, Department of Materials Science and Engineering, and Department of Biomedical Engineering, City University of Hong Kong, Tat Chee Avenue, Kowloon, Hong Kong, China

ARTICLE INFO

Keywords:
Vernier effect
Optical fiber sensors
Fabry-Perot interferometer

ABSTRACT

A major challenge in Vernier-effect-based optical fiber sensors lies in their complex and costly fabrication processes. To address this issue, we propose and demonstrate a dual-parallel Fabry-Pérot interferometer (FPI) optical fiber strain sensor. The cavity length of the bubble-based FPI can be precisely tuned via iterative fusion splicing with an electric arc, enabling straightforward and cost-effective implementation of the Vernier effect. The sensor achieves a strain sensitivity of 866.6 pm/με within the 0–300 με range, representing a 29.93-fold enhancement compared to a single FPI. Additionally, it exhibits a temperature sensitivity of 11.91 pm/°C and a low temperature cross-sensitivity of 0.01374 με/°C over 25–150 °C, fulfilling practical strain monitoring requirements under significant temperature fluctuations.

1. Introduction

Optical fiber sensors typically monitor changes in physical parameters such as temperature, stress, curvature, and refractive index by modulating the amplitude, polarization, frequency, and phase of the incident light [1–5]. The Vernier effect is widely adopted by interferometric fiber optic sensors due to its superior sensitivity enhancement capability and simple implementation [6–10]. The mechanism relies on integrating two interferometers—commonly termed the Reference Interferometer (RI) and Sensing Interferometer (SI)—in series or parallel to generate two closely matched Free Spectral Ranges (FSRs), thereby emulating a pair of Vernier scales. This results in the formation of a Vernier envelope peak that is highly sensitive to environmental changes, enabling high-sensitivity monitoring thereby facilitating the monitoring of physical parameters such as temperature [11,12], strain [13,14], and refractive index [15,16] with high sensitivity. However, this sensitivity enhancement approach introduces challenges, including multi-parametric cross-talk and reduced interference contrast.

Fabry-Pérot Interferometers (FPIs) are renowned for their precise FSR control, simple configuration, and low temperature cross-sensitivity, making them a preferred choice for Vernier-effect-based optical fiber strain sensors [17–19]. To generate stable interference spectra, FPIs often require specialized fiber structures such as hollow-core Photonic Crystal Fibers (PCFs) [20], solid-core PCFs [21,22], and silica capillaries [23,24]. These structures typically necessitate complex fabrication techniques, such as precision fiber cutting [25–27] or femtosecond laser micromachining [28,29], which involve complex subsystems including precision motion platforms, imaging modules and feedback control. Furthermore, the sensitivity enhancement capability of the Vernier effect depends on the relationship between the FSRs of the RI and SI: their product must be sufficiently large or their difference sufficiently small. Achieving this requires a smaller FP cavity to attain both a higher extinction ratio and a wider FSR, but such miniaturization significantly complicates the manufacturing process and the matching of the RI and SI parameters.

Herein, we present a simple, cost-effective method for fabricating a Vernier-effect-based optical fiber sensor capable of highly sensitive strain measurements with minimal temperature cross-sensitivity. The SI and RI, fabricated via fusion splicing, are coupled in parallel. The RI, implemented as a bubble microcavity, allows rapid cavity length tuning through iterative electric arc discharges (less than 10 iterations, 5–10 min per sensor, >90 % success rate) until the Vernier envelope peaks

* Corresponding author.
E-mail address: msm-liu@126.com (C. Liu).

https://doi.org/10.1016/j.infrared.2025.105939
Received 18 April 2025; Received in revised form 22 May 2025; Accepted 26 May 2025
Available online 27 May 2025

with optimal sensitivity. Experimental results demonstrate that the sensor achieves an ultra-high strain sensitivity of 866.6 pm/με within the 0–300 με range—a 29.6-fold improvement over conventional single FPIs—while maintaining a high interference contrast of 21.27 dB. Additionally, the sensor exhibits a temperature sensitivity of 11.91 pm/°C and a temperature cross-sensitivity of 0.01374 με/°C over the range of 25–150 °C.

2. Principle and fabrication

To evaluate the strain response of the device, we designed an experimental setup as shown in Fig. 1. A Supercontinuum (SC) source (NKT Photonics SuperK EXTREME; spectral range: 400–2400 nm, output power: 100 mW) was connected to a 50:50 fiber coupler, splitting light equally into the SI and RI. The reflected beams from both interferometers were recombined through the coupler and directed into an Optical Spectrum Analyzer (OSA; Yokogawa AQ6370D, operational range: 600–1700 nm, resolution: 0.02 nm) for real-time spectral monitoring. The SI was positioned between two three-dimensional translation stages spaced 40 cm apart. With a minimum displacement resolution of 10 μm, the translation stages could apply strain increments of 25 με to the sensor. In the SI configuration, the bubble microcavity features thin walls where axial strain induces minute deformations.

Here, M_1 and M_2 represent the two reflective surfaces of the air bubble within the optical fiber. When broadband light from the SC reaches the first reflective surface M_1, the initial reflected light intensity is $\boldsymbol{I_0}$, producing a first reflection intensity $\boldsymbol{I_1}$. A portion of the light transmits through M_1 and undergoes a second reflection at surface M_2 with intensity $\boldsymbol{I_2}$. These two reflected beams then interfere through core-mode coupling in the single-mode fiber (SMF).

The reflection spectrum of the Sensing Interferometer (SI) can be expressed as [30]:

$$I_{SI} = I_1 + I_2 + 2\sqrt{I_1 I_2}\cos\left(\frac{4\pi n_{SI} L_{SI}}{\lambda} + \phi_0\right), \tag{1}$$

where $\boldsymbol{I_1} = \boldsymbol{R_1}$, $\boldsymbol{I_2}$=(1 − $\boldsymbol{R_1}$) (1 − $\boldsymbol{\kappa}$), $\boldsymbol{R_1}$ and $\boldsymbol{R_2}$ are the reflectance of M_1 and M_2 respectively, $\boldsymbol{\kappa}$ represents the total transmission loss of the sensing cavity, λ is the vacuum wavelength, $\boldsymbol{n_{SI}}$ is the refractive index of the cavity medium, $\boldsymbol{L_{SI}}$ is the cavity length, and $\boldsymbol{\phi_0}$ is the initial phase. At interference minima (dips), the phase condition satisfies:

$$\frac{4\pi n_{SI} L_{SI}}{\lambda_m} + \phi_0 = (2m+1)\pi, \tag{2}$$

where $\boldsymbol{m}$ is an integer and $\boldsymbol{\lambda m}$ is the wavelength of the $\boldsymbol{m}$-th order dip. Solving for $\boldsymbol{\lambda m}$:

$$\lambda_m = \frac{4 n_{SI} L_{SI}}{2m+1}. \tag{3}$$

The FSR of the SI is derived as:

$$FSR_{SI} = \lambda_{m-1} - \lambda_m \approx \frac{\lambda^2}{2 n_{SI} L_{SI}}. \tag{4}$$

When strain ($\boldsymbol{\varepsilon}$) is applied, the cavity length $\boldsymbol{L_{SI}}$ elongates ($\boldsymbol{\Delta L_{SI}}$) while the medium's refractive index remains constant, leading to a redshift of dip wavelengths [31,32]:

$$\varepsilon = \frac{\Delta L_{SI}}{L_{SI}}, \tag{5}$$

where $\boldsymbol{\varepsilon}$ is a dimensionless quantity characterizing relative deformation.

In contrast, the Reference Interferometer (RI) is intentionally fabricated with thicker bubble walls to minimize strain-induced perturbations. In this configuration, M_3 and M_4 denote the two reflective surfaces, generating first and second reflection intensities $\boldsymbol{I_3}$ and $\boldsymbol{I_4}$ respectively. Its reflection spectrum and FSR are given by:

$$I_{RI} = I_3 + I_4 + 2\sqrt{I_3 I_4}\cos\left(\frac{4\pi n_{RI} L_{RI}}{\lambda} + \phi_0\right), \tag{6}$$

$$FSR_{RI} \approx \frac{\lambda^2}{2 n_{RI} L_{RI}}, \tag{7}$$

Where $\boldsymbol{n_{RI}}$ and $\boldsymbol{L_{RI}}$ are the RI's refractive index and cavity length, respectively.

Under parallel Vernier coupling, the superimposed spectrum exhibits a modulated envelope:

$$I = I_{SI} + I_{RI} = A + B\cos\left(\frac{4\pi(L_{SI} - L_{RI})}{\lambda}\right), \tag{8}$$

where $\boldsymbol{A}$ is a constant offset and $\boldsymbol{B}$ the envelope amplitude. The envelope's FSR and dip wavelength ($\boldsymbol{\lambda_{env}}$) are:

$$\lambda_{env} = \frac{4(n_{RI} L_{RI} - n_{SI} L_{SI})}{2m+1}, \tag{9}$$

$$FSR_{env} = \frac{FSR_{SI} \times FSR_{RI}}{|FSR_{SI} - FSR_{RI}|}. \tag{10}$$

The sensitivity magnification factors $\boldsymbol{M_{SI}}$ and $\boldsymbol{M_{RI}}$ relative to SI and RI are defined as:

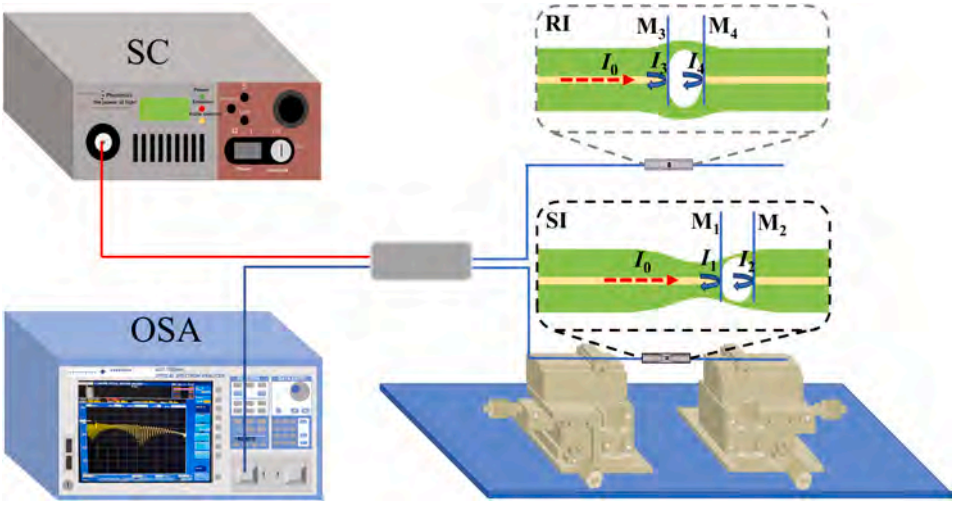

Fig. 1. Experimental setup for the strain measurement.

$$M_{SI} = \frac{FSR_{env}}{FSR_{SI}} = \frac{FSR_{RI}}{|FSR_{RI} - FSR_{SI}|},\ M_{RI} = \frac{FSR_{env}}{FSR_{RI}} = \frac{FSR_{SI}}{|FSR_{RI} - FSR_{SI}|}. \quad (11)$$

Then the displacement of the envelope curve is affected by both SI and RI, which can be defined as [33]:

$$\Delta\lambda_{env} = \Delta\lambda_{RI}M_{RI} - \Delta\lambda_{SI}M_{SI}. \quad (12)$$

Thus, the Vernier-enhanced strain sensitivity becomes:

$$S_{env} = S_{SI}M_{SI} - S_{RI}M_{RI}. \quad (13)$$

When only the SI is strained ($S_{RI} = 0$), this simplifies to:

$$S_{env} = S_{SI}M_{SI}. \quad (14)$$

The fabrication process of the sensor is illustrated in Fig. 2. The pretreatment procedure shown in Fig. 2(a) consists of the following steps: First, a SMF (Corning SMF-28) is precisely cleaved and mounted in the fiber holder of a commercial fusion splicer (Fujikura 80S). Second, the fiber end face is reshaped into a smooth hemispherical surface via arc discharge to increase its surface area. Third, the fiber end is dipped in glycerol to facilitate microbubble formation. Finally, the left and right fiber ends are brought into slight contact using the splicer's stepper motor before fusion (standard discharge power, 800 ms), creating a microbubble at the joint during the fusion process. The two pretreated fibers are then connected to the optical path shown in Fig. 1, enabling real-time spectral monitoring during sensor fabrication. There are two keys to the pretreatment process: The melted, smooth curved fiber end enhances surface tension, improving liquid dipping/adsorption capability; Glycerol is selected as it is non-volatile and strongly adhesive, allowing extended operation time. Our experiments show various liquids can be used, with preference given to those with low volatility and strong adhesion properties.

Fig. 2(b) illustrates the manufacturing process of SI. First, by prolonging the discharge time and applying axial tension to the optical fiber deviated from the central position, the microbubbles at the junction further expand. Subsequently, through shortening the discharge time and applying axial pressure to the centrally positioned optical fiber, the microbubbles at the junction evolve into a rectangular-like structure that slightly protrudes from the cladding. Real-time spectral feedback of interference contrast governs adaptive process optimization, including iterative compression cycles and dynamic tension readjustments. Fig. 3 (a) presents the optical micrograph and geometric parameters of the high-sensitivity FPI, where the microbubble exhibits an average minimum wall thickness of 1.75 μm, axial length of 58.8 μm, and longitudinal dimension of 68.5 μm, as captured by an Olympus CX31 optical microscope at 40× magnification with dimensional analysis performed

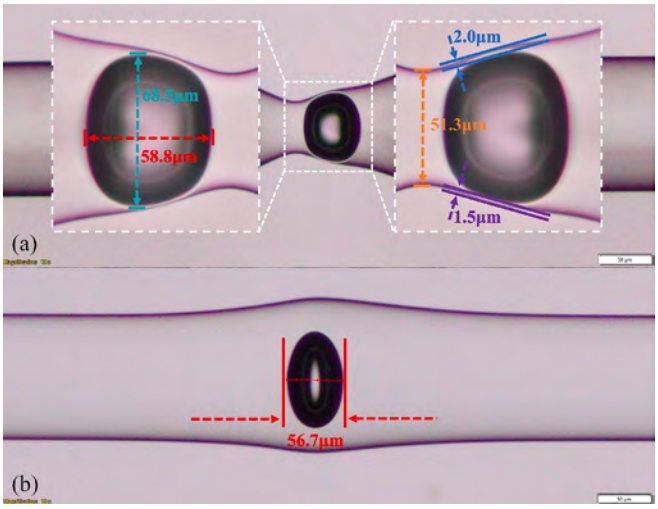

Fig. 3. Microscopic image of the device.

using the cellSens entry measurement software. To enhance imaging clarity, the sample was immersed in a water droplet during microscopic characterization.

The fabrication process of the Reference Interferometer (RI) is detailed in Fig. 2(c). Crucially, RI fabrication commences only after completing the SI fabrication. Initial microbubble expansion at fiber joints is achieved through sustained arc discharge combined with axial tension applied to centrally aligned fibers. Unlike sensing interferometers requiring high air-filling ratios or reduced cladding thickness, the RI design prioritizes stability over sensitivity enhancement. This enables a highly controllable process achieved through multiple low-power, short-duration discharges (<100 ms) while monitoring real-time spectra, with iterative axial pressure/tension adjustments until distinct Vernier spectral features emerge. The arc discharge locally softens bubble cladding material, enabling precise cavity length tuning via micron-scale motorized fixture displacements to match the sensing cavity dimensions.

Fig. 3(b) shows a low-sensitivity FPI with 56.7 μm cavity length specifically engineered for SI matching. Experimental validation demonstrated 90 % success rate (18/20) in generating clear Vernier envelopes through this approach. The inherent adaptability of FP cavity length modification substantially simplifies Vernier effect implementation compared to conventional methods. Fig. 4 systematically documents the RI fabrication stages through sequential microscopic images

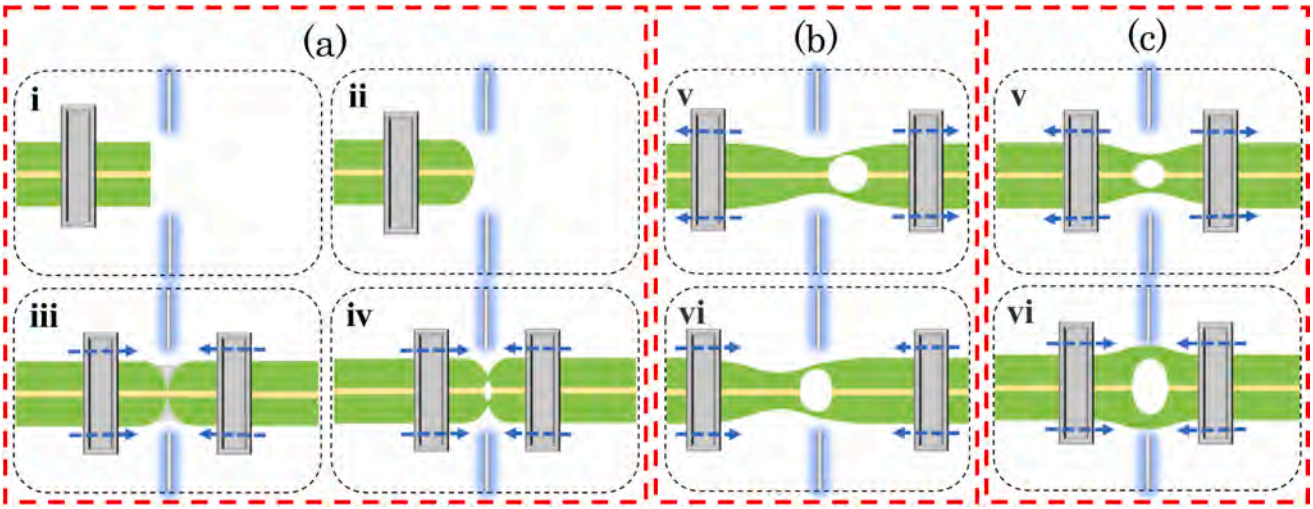

Fig. 2. Schematic diagram of the fabrication process.

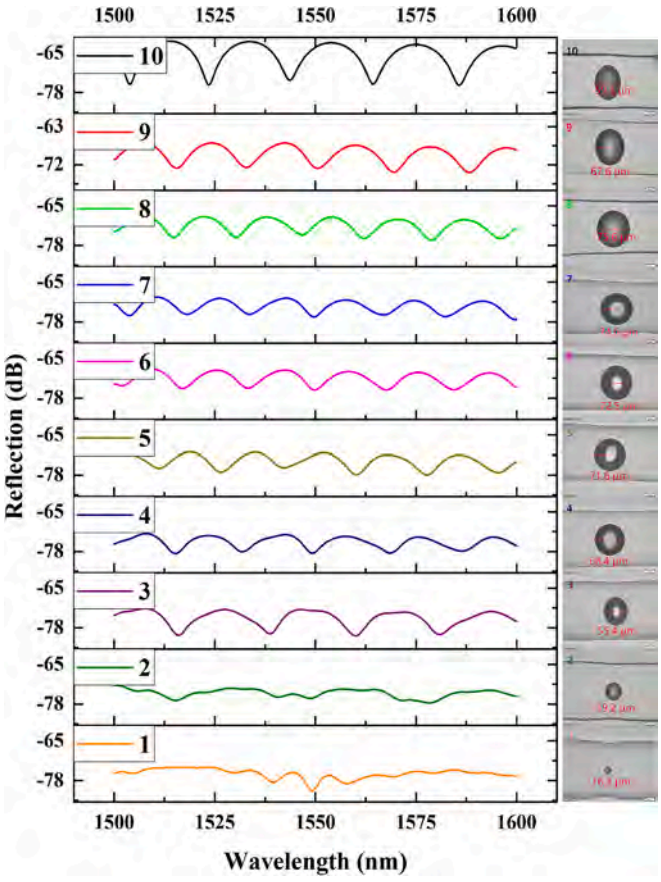

Fig. 4. Production of microscopic images of the various stages of the reference interferometer and the corresponding interference spectra.

(1–10) with corresponding spectral evolution. The cavity length tuning mechanism combines controlled microbubble release with selective mechanical manipulation (compression/extension), allowing micron adjustments under varying operational conditions.

3. Experimental results

The wavelength fitting curves for the SI and RI sensors shown in Fig. 3 in the range of 0–300 με are shown in Fig. 5. The strain sensitivities of SI and RI are 28.95 pm/με and 0.8 pm/με, respectively. The difference in the sensitivities is attributed to the difference in the structure of the FP cavities, which helps to avoid the effect of the RI on the strain measurements after the vernier effect.

Fig. 6(a) displays the reflectance spectra of the sensor under varying strains, with the Vernier envelope extracted from raw interference spectra using OriginPro 2021′s built-in envelope tool. Key parameters include: (1) a 200-point moving average smoothing method, corresponding to a 4 nm window (200 × 0.02 nm wavelength spacing); (2) automatic local maxima detection via threshold filtering (minimum intensity change: 3 dB). This parameter selection was optimized based on the Vernier envelope's FSR ($\boldsymbol{FSR}_{\mathbf{env}}$ = 487.1 nm) to balance noise suppression and spectral feature preservation. The validity of the extracted envelope was confirmed by comparing experimental peak wavelengths with theoretical predictions (Fig. 6c). Fig. 6(b) illustrates the linear strain-wavelength fitting results. The Vernier envelope exhibits a pronounced redshift with increasing strain, as evidenced by Dip 1 (purple arrow) shifting from 1036.9 nm to 1511.22 nm, yielding a sensitivity of 588.87 pm/με. Spectral analysis reveals suppressed Vernier modulation between 900–1100 nm, resulting in nonlinear wavelength responses below 300 με. Within the 0–300 με range, Dip 2 (blue arrow) demonstrates linear redshift behavior from 1384.22 nm to 1643.92 nm, achieving enhanced sensitivity of 866.6 pm/με. Notably, Dip 1 surpasses Dip 2 at 600 με (vs. 0 με reference), establishing an optimized detection window of 500–600 με where stable Vernier modulation dominates.

To elucidate the Vernier envelope formation mechanism, Fig. 6(c) compares the raw spectra of the SI and RI between 1100–1700 nm with their superimposed parallel-coupled spectrum. Both uncoupled SI and RI spectra exhibit periodic sinusoidal interference patterns with comparable fringe contrasts, displaying free spectral ranges of $\boldsymbol{FSR}_{\mathbf{S}}$ = 16.28 nm and $\boldsymbol{FSR}_{\mathbf{R}}$ = 16.84 nm, respectively. Calculated bubble cavity lengths derived from Eqs. (2) and (3) yield $\boldsymbol{L}_{\mathbf{S}}$ = 58.67 μm and $\boldsymbol{L}_{\mathbf{R}}$ = 56.73 μm, showing excellent agreement with microscopic measurements in Fig. 2. The lower Vernier envelope demonstrates pronounced modulation depth with 21.28 dB interference contrast. Experimental and theoretical envelope ***FSR*** values align closely at 487.1 nm (measured) versus 489.56 nm (calculated via Eq. (7). While the spectrometer's operational bandwidth limits observable spectral shifts of Dip 2 to 300 με, theoretical extrapolation based on the FSR-to-sensitivity ratio (***FSR/S***) suggests an extended effective detection range of 569.08 με. This extension derives from the periodic nature of Vernier modulation, where envelope periodicity enables strain quantification beyond immediate spectral window constraints.

Sensor measurement uncertainty was validated by comparing strain sensitivities during ascending (0 → 300 με) and descending (300 → 0 με) loading cycles, as shown in Fig. 7(a). Axial strain was applied in 50 με increments at 5-minute intervals using a precision displacement stage, with spectral responses recorded throughout the process (see inset in Fig. 7a). Linear regression analysis revealed strain sensitivities of 849.59 ± 4.3 pm/με (mean ± 1σ) during loading and 858.47 ± 4.5 pm/με (mean ± 1σ) during unloading phases. The sensor demonstrated exceptional stability across multiple tensile cycles, evidenced by a

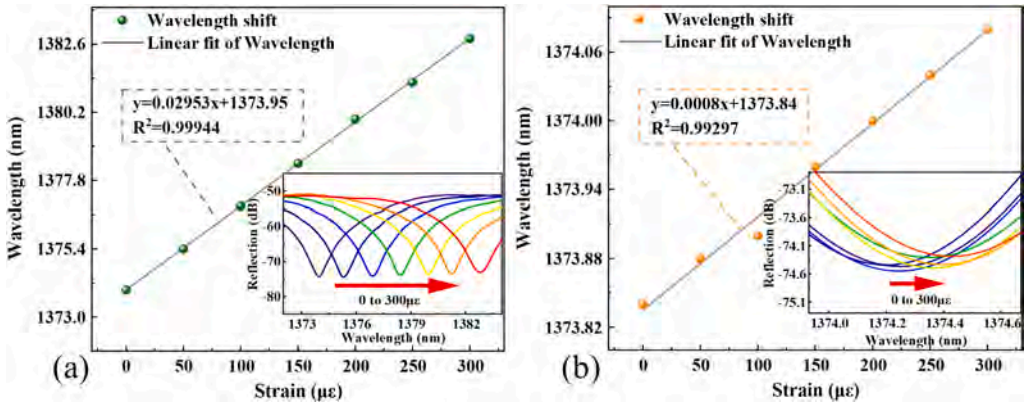

Fig. 5. Interference spectra and linear fits corresponding to the (a) SI and (b) RI.

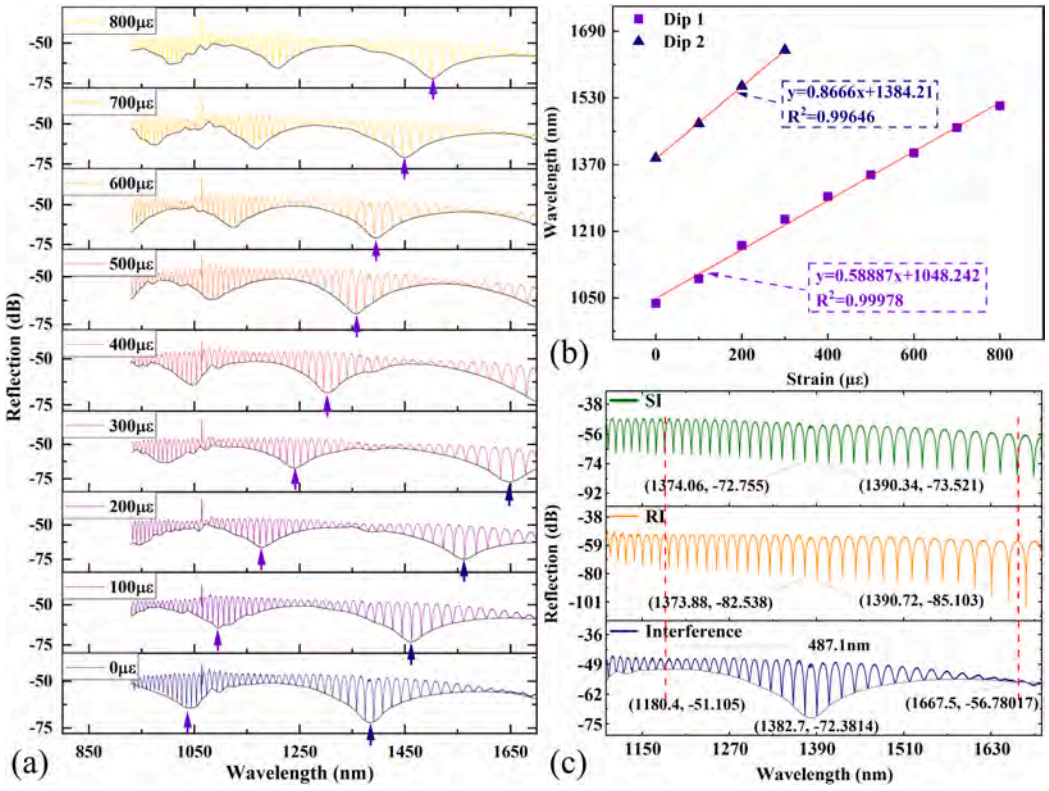

Fig. 6. (a) Superimposed spectra of SI, RI and after parallel connection; (b) Strain sensitivity fitting of the vernier envelope; (c) Interference spectra for different strains.

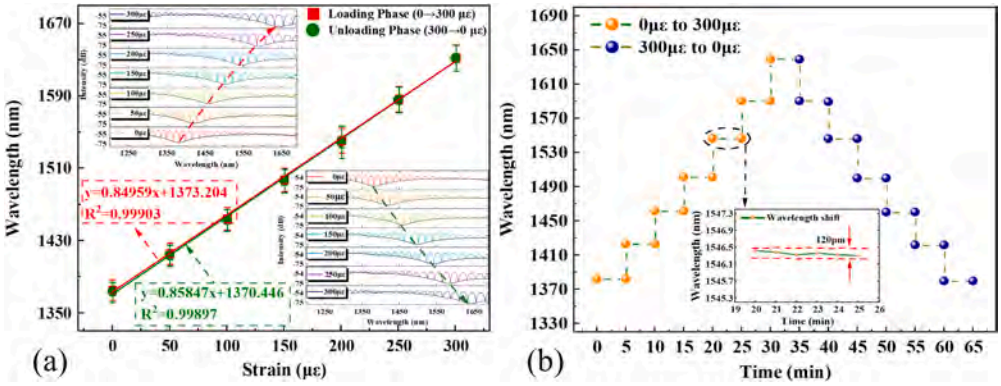

Fig. 7. (a) Strain response during loading (red, 0 → 300 με) and unloading (black, 300 → 0 με) cycles. Solid lines: linear fits. Error bars: ±3σ (n = 5, magnified 3 × for visibility). (b) Wavelength change of the Vernier envelope at different times. (For interpretation of the references to colour in this figure legend, the reader is referred to the web version of this article.)

maximum spectral deviation of 120 pm over repeated measurements (Fig. 7(b) inset), corresponding to a minimum resolvable strain of approximately 0.14 με. The minor sensitivity discrepancy likely originates from two factors: (1) inherent interferometer noise amplified through Vernier modulation, and (2) micrometer-scale positioning tolerances (±0.5 με) in the manual 3D translation system.

The axial length of fiber-embedded microbubbles undergoes temperature- and stress-dependent variations, inducing corresponding shifts of interference peaks in Fabry-Pérot interferometric spectra. To eliminate mechanical displacement artifacts during thermal characterization, both sensing (SI) and reference interferometers (RI) were immobilized on optical-grade glass substrates using polyimide tape (thermal expansion coefficient: 0.55 × 10–6/°C) and subjected to controlled heating from 25 °C to 150 °C with 25 °C increments. Fig. 8(a-b) depict spectral evolution, while Fig. 8(c) quantifies temperature sensitivities through linear regression: 0.99 pm/°C for SI, 1.38 pm/°C for RI, and 11.91 pm/°C for the Vernier envelope. The sublinear temperature sensitivity amplification originates from coordinated thermal expansion of SI and RI cavities – both elongating under heating due to matched thermal expansion coefficients, as confirmed by COMSOL Multiphysics simulations (solid mechanics module, Fig. 8d). This codirectional length change produces wavelength shifts ($\Delta\lambda_{SI}$ and $\Delta\lambda_{RI}$) with identical polarity, thereby suppressing Vernier envelope displacement through superposition (Eq. (12). Consequently, the temperature-strain cross-sensitivity reduces to 0.01374 με/°C ($S_{env,\ T}$ / $S_{env,\ \varepsilon}$), demonstrating exceptional temperature compensation capability inherent to the dual-FPI parallel architecture [34].

The properties of our strain sensor are compared to those of similar high-sensitivity strain sensors utilizing the Vernier effect. Table 1 shows that our sensor has ultra-high strain sensitivity and low-temperature

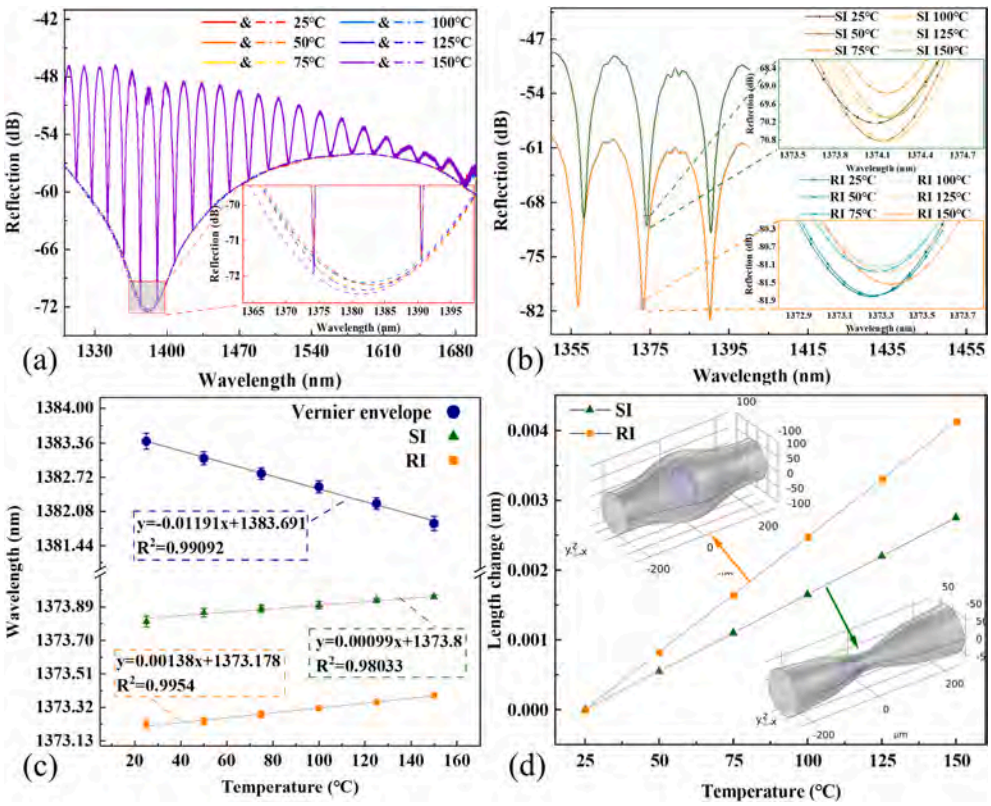

Fig. 8. Interference spectra of the (a) vernier envelope with (b) SI and RI at different temperatures; (c) linear fit to temperature sensitivity; (d) change in cavity length at different temperatures.

Table 1
Comparison of our sensor with previously reported strain sensors.

Refs.	Solution	Strain sensitivity (pm/με)	Effective detection range (με)	Temperature cross-Sensitivity (με/°C)	Strain Resolution (με)
[24]	FPIs by precision cut capillaries	1307 pm/με	0–40 με	–-	0.193 με
[29]	FPIs by fs laser	236.32 pm/με	0–423.16 με	0.0292 με/°C	–-
[18]	MZI and FPI by precision cut capillaries	−649.2 pm/με	0–50 με	0.0089 με/°C	0.1 με
[34]	FPI by precision cut capillaries	940.02 pm/με	0–40 με	0.0005 με/°C	0.07
[37]	CFBG-FPI by fs laser	123.8 pm/με	0–791 με	0.14 με/°C	–-
[36]	Mechanical amplifier FBG	5.44 pm/με	0–580 με	–-	1.98–4.25 με
This work	FPIs by fusion splicer	866.6 pm/με	0–569.08 με	0.01374 με/°C	0.14 με

sensitivity over a wide strain range. Compared to commercial FBG strain sensors, our device achieves 10 × higher resolution (0.14 με vs. 1–4.25 με [35,36]) due to Vernier-amplified sensitivity, albeit with a narrower dynamic range. This makes it particularly suitable for microstrain monitoring in precision engineering applications.

4. Conclusion

We present an optical fiber strain sensor based on the Vernier effect. The fusion splicer-based FPI is able to adjust the length of the micro-cavity quickly, thus reducing the difficulty of matching the FSR_S with the FSR_R. The experimental results show that the sensor has an ultra-high strain sensitivity of 866.6 pm/με, which is 29.93 times higher than that of a single FPI, as well as a high detection range of 569.08 με. The temperature sensitivity and cross-sensitivity of the sensor are 11.91 pm/°C and 0.01374 με/°C, respectively, in the temperature range of 25 °C −150 °C. The sensor's hermetic silica structure and rigid mounting make it particularly suitable for stable environments like civil infrastructure monitoring, where humidity/pressure fluctuations are typically negligible compared to strain/temperature variations.

CRediT authorship contribution statement

Chao Liu: Writing – review & editing, Funding acquisition, Conceptualization. **Jianxin Wang:** Writing – original draft, Methodology, Data curation. **Jingwei Lv:** Software. **Xinping Song:** Investigation. **Wei Liu:** Visualization. **Qiang Liu:** Supervision. **Renfeng Li:** Validation. **Liangliang Li:** Resources. **Zao Yi:** Funding acquisition. **Paul K. Chu:** Writing – review & editing, Funding acquisition.

Declaration of competing interest

The authors declare that they have no known competing financial interests or personal relationships that could have appeared to influence the work reported in this paper.

Acknowledgement

This work was jointly supported by the National Natural Science

Foundation of China [12304480], Local Universities Reformation and Development Personnel Training Supporting Project from Central Authorities, Natural Science Foundation of Heilongjiang Province [LH2021F007], Heilongjiang Provincial Natural Science Foundation of China [JQ2023F001], China Postdoctoral Science Foundation funded project [2020 M670881], as well as City University of Hong Kong Donation Research Grants [DON-RMG 9229021 and 9220061].

Data availability

No data was used for the research described in the article.

References

[1] J. Wang, X. Lu, C. Mi, Q. Yin, J. Lv, L. Yang, W. Liu, Z. Yi, Q. Liu, P.K. Chu, Ultra-high sensitivity photonic crystal fiber sensor based on dispersion turning point sensitization of surface plasmonic polariton modes for low RI liquid detection, Opt. Express 32 (19) (2024) 32895–32908.
[2] W. Liu, Y. Shi, Z. Yi, C. Liu, F.M. Wang, X.L. Li, J.W. Lv, L. Yang, P.K. Chu, Surface plasmon resonance chemical sensor composed of a microstructured optical fiber for the detection of an ultra-wide refractive index range and gas-liquid pollutants, Opt. Express 29 (25) (2021) 40734–40747.
[3] H. Fu, Z. Sheng, W. Gao, Y. Guo, B. Wang, X. Wang, S. Lou, Ultra-high sensitive dual-parameter sensor based on double-hole fiber for simultaneous detection of magnetic field and temperature, Opt. Express 32 (11) (2024) 20175–20193.
[4] W. Luo, Y. Chen, A. Xiao, Q. Ling, B. Zhang, S. Luo, Z. Yu, Y. Zhang, Z. Guan, D. Chen, Three-core fiber-based temperature-insensitive twist sensor, Opt. Commun. 554 (2024) 130229.
[5] Y. Li, Z. Yu, Q. Ling, Q. Zhang, H. Wu, J. Yang, Y. Zhang, H. Chen, B.-M. Mao, D. Chen, Temperature-insensitive vector curvature sensor based on four-core fiber offset structure, Infrared Phys. Technol. 140 (2024) 105368.
[6] X. Zhu, C. Jiang, H. Chen, Y. Wang, X. Guo, S. Sun, H. Huang, Ultrasensitive gas pressure sensor based on two parallel Fabry-Perot interferometers and enhanced Vernier effect, Opt. Laser Technol. 158 (2023) 108755.
[7] J. Song, S. Sun, C. Jiang, N. Chen, W. Jiang, C. Liu, J. Ren, S. Wang, Ultra-sensitive temperature and pressure sensor based on PDMS-based FPI and Vernier effect, Opt. Lett. 48 (7) (2023) 1674–1677.
[8] H. Li, M. Xu, H. Song, A. Zhou, A high-sensitivity air pressure sensor with short desorbing time, Opt. Laser Technol. 158 (2023) 108855.
[9] S. Zhang, L. Yin, Y. Zhao, A. Zhou, L. Yuan, Bending sensor with parallel fiber Michelson interferometers based on Vernier-like effect, Opt. Laser Technol. 120 (2019) 105679.
[10] S. Duan, S. Pu, X. Lin, W. Liu, Z. Hao, C. Zhang, J. Fu, S. Han, Enhanced sensitivity of temperature and magnetic field sensor based on FPIs with Vernier effect, Opt. Express 32 (1) (2023) 275–286.
[11] Y. Zhao, M. Dai, Z. Chen, X. Liu, M.A. Gandhi, Q. Li, H. Fu, Ultrasensitive temperature sensor with Vernier-effect improved fiber Michelson interferometer, Opt. Express 29 (2) (2021) 1090–1101.
[12] W. Chen, J. Wang, Y. Liu, T. Geng, C. Lu, X. Zeng, J. Hao, J. Zhou, Y. Yan, Q. Yan, Study on Vernier effect of orthogonal Mach-Zehnder interferometers based on Polarization-maintaining fiber, Opt. Laser Technol. 165 (2023) 109599.
[13] J. Tian, Z. Li, Y. Sun, Y. Yao, High-sensitivity fiber-optic strain sensor based on the Vernier effect and separated Fabry–Perot interferometers, J. Lightwave Technol. 37 (21) (2019) 5609–5618.
[14] C. Liu, H. Chen, Q. Chen, Z. Gao, B. Wu, X. Fan, M. Ma, Sagnac interferometer-based optical fiber strain sensor with exceeding free spectral measurement range and high sensitivity, Opt. Laser Technol. 159 (2023) 108935.
[15] Z. Xu, Q. Sun, B. Li, Y. Luo, W. Lu, D. Liu, P.P. Shum, L. Zhang, Highly sensitive refractive index sensor based on cascaded microfiber knots with Vernier effect, Opt. Express 23 (5) (2015) 6662–6672.
[16] T. Yao, S. Pu, Y. Zhao, Y. Li, Ultrasensitive refractive index sensor based on parallel-connected dual Fabry-Perot interferometers with Vernier effect, Sens. Actuators, A 290 (2019) 14–19.
[17] T. Nan, B. Liu, Y. Wu, J. Wang, Y. Mao, L. Zhao, T. Sun, J. Wang, Ultrasensitive strain sensor based on Vernier-effect improved parallel structured fiber-optic Fabry-Perot interferometer, Opt. Express 27 (12) (2019) 17239–17250.
[18] Z. Wang, S. Jiang, P. Yang, W. Wei, W. Bao, B. Peng, High-sensitivity and high extinction ratio fiber strain sensor with temperature insensitivity by cascaded MZI and FPI, Opt. Express 31 (5) (2023) 7073–7089.
[19] L.G. Abbas, Vernier effect-based strain sensor with cascaded Fabry–Perot interferometers, IEEE Sens. J. 20 (16) (2020) 9196–9201.
[20] C. Zuo, J.T. Luo, T.F. Wang, Y.Z. Wang, J. Zhu, X.Q. Wu, J.H. Shi, B.L. Yu, Ultrasensitive Temperature and Strain Sensor Based on a Hybrid Fiber Interferometer With the Vernier Effect, IEEE Sens. J. 24 (13) (2024) 20713–20718.
[21] G. Zhang, W. Zhang, L. Gui, S. Li, S. Fang, C. Zuo, X. Wu, B. Yu, Ultra-sensitive high temperature sensor based on a PMPCF tip cascaded with an ECPMF Sagnac loop, Sens. Actuators, A 314 (2020) 112219.
[22] Y. Kong, Y. Ruan, H. Ebendorff-Heidepriem, Z. Xu, X. Shu, Microstructured optical fibers based hybrid Fabry–Pérot interferometer structure for improved strain sensing by Vernier effect, Ieee T Instrum Meas 71 (2022) 1–14.
[23] L. Zhao, S. Hao, Y. Chen, E. Zhao, C. Xing, J. Fan, J. Tang, Simultaneous measurement of strain and temperature based on fiber sensor with Vernier effect, Opt. Laser Technol. 157 (2023) 108670.
[24] X. Zhao, Y. Zhang, W. Zhang, Z. Li, Y. Yue, T. Yan, Ultrasensitive Fabry–Perot strain sensor based on Vernier effect and tapered FBG-in-hollow silica tube, IEEE Sens. J. 21 (3) (2020) 3035–3041.
[25] Z.J. Jiang, F.G. Wu, J. Yang, K.H. Wen, P.B. Xu, Z.J. Yu, J.Q. Sun, Y.C. Wang, Y. W. Qin, Combined-Vernier effect based on hybrid fiber interferometers for ultrasensitive temperature and refractive index sensing, Opt. Express 30 (6) (2022) 9578–9589.
[26] W. Luo, Y. Wang, Q. Ling, X. Zhu, X. Wang, Z. Gu, H. Chen, Z. Yu, Y. Zhang, H. Wang, D. Chen, Simultaneous bending and temperature measurement based on a superimposed fiber grating sensor, Infrared Phys. Technol. 140 (2024) 105371.
[27] X. Jiang, Q. Zhang, Q. Ling, Y. Li, J. Xu, Y. Zhang, H. Chen, Z. Gu, Z. Yu, Z. Guan, Integrated all-fiber sensor for simultaneous measurements of curvature and temperature, IEEE Sens. J. 24 (6) (2024) 7844–7849.
[28] J. Deng, D. Wang, Ultra-sensitive strain sensor based on femtosecond laser inscribed in-fiber reflection mirrors and Vernier effect, J. Lightwave Technol. 37 (19) (2019) 4935–4939.
[29] D. Wang, X. Cui, H. Zhang, J. Deng, Ultrasensitive Strain Sensing by Using Two Parallel Structured Fabry-Perot Interferometers in Cascaded Connection, J. Lightwave Technol. 39 (5) (2020) 1504–1508.
[30] J. Lv, W. Li, J. Wang, X. Lu, Q. Li, Y. Ren, Y. Yu, Q. Liu, P.K. Chu, C. Liu, High-sensitivity strain sensor based on an asymmetric tapered air microbubble Fabry-Pérot interferometer with an ultrathin wall, Opt. Express 32 (11) (2024) 19057–19068.
[31] F. Mumtaz, M. Roman, B. Zhang, J. Huang, Assembly-free ultra-sensitive miniaturized strain sensor based on an asymmetric optical fiber taper, Measurement 211 (2023) 112655.
[32] C.D. Butter, G.B. Hocker, Fiber optics strain gauge, Appl Optics 17 (18) (1978) 2867–2869.
[33] P. Yang, S. Jiang, Z. Wang, B. Peng, Hybrid Interferometer Sensor Based on the Enhanced Vernier Effect for the Simultaneous Measurement of Strain and Temperature, Ieee T Instrum Meas 73 (2024) 1–10.
[34] Z. Wang, W. Bao, P. Yang, S. Jiang, Y. Zhang, X. Zhu, W. Wei, B. Peng, Highly Sensitive Strain Sensor Based on the Vernier Effect With High Extinction Ratio and Low-Temperature Cross-Sensitivity by Compact Double FPI, IEEE Sens. J. 24 (6) (2024) 7896–7904.
[35] H. Guo, G. Xiao, N. Mrad, J. Yao, Fiber optic sensors for structural health monitoring of air platforms, Sensors 11 (4) (2011) 3687–3705.
[36] K. Yao, Q. Lin, Z. Jiang, N. Zhao, B. Tian, G.-D. Peng, Design and analysis of a combined FBG sensor for the measurement of three parameters, IEEE Trans. Instrum. Meas. 70 (2021) 1–10.
[37] X.P. Pan, H.E. Yang, S.R. Liu, B. Wang, M.M. Gao, Q. Guo, Q.D. Chen, H.B. Sun, Y. S. Yu, High Sensitivity Fiber Optic Strain Sensor Based on CFBG-FPI and Vernier Effect, J. Lightwave Technol. 41 (21) (2023) 6831–6837.